

**Dependence of scalar mixing on initial conditions in turbulent channel flow**Milind Singh , Emmanuel Germaine, and Laurent Mydlarski *Department of Mechanical Engineering, McGill University, Montréal, Québec H3A 0C3, Canada*Luca Cortelezzi *Department of Aerospace Science and Technology, Politecnico di Milano, 20156 Milano, Italy*

(Received 17 August 2023; accepted 13 November 2023; published 19 December 2023)

Turbulent scalar mixing occurs within a wide variety of natural and engineering flows. Predicting and controlling the scalar concentration(s) within these flows can yield immediate benefits to numerous applications across many fields. To that end, a better understanding of the effects of scalar-field initial conditions on the evolution(s) of scalar fields is required to either promote or delay the rate at which mixing occurs. Direct numerical simulations are employed herein to simulate the evolution in time of the hydrodynamic and (passive) scalar fields within a fully developed turbulent channel flow. The effects of the scalar field initial conditions are studied by analyzing the evolution of the scalar field subject to three different initial conditions with interfaces oriented normal to the streamwise, wall-normal, and transverse directions. Particular emphasis is placed on the scalar variance and dissipation rate budgets, including the evolutions of their constituent terms. The fastest mixing occurs for the initial condition in which the interface is aligned normal to the mean velocity vector. The rapid mixing in this case is associated with higher rates of production and destruction of the scalar dissipation, as well as strong advection and stretching of the interface by the mean flow. In addition to better mixing arising from the stronger turbulence near the wall, enhanced mixing is correlated with having the edge of an interface along a channel wall, such that a large distortion of the initial interface arises from the combined effects of the no-slip condition at the channel walls with the advection of the interface by the mean flow in the region between the walls. To maximize this effect, it is recommended that scalar interfaces be aligned normal to the mean velocity vector to promote mixing within internal flows.

DOI: [10.1103/PhysRevFluids.8.124605](https://doi.org/10.1103/PhysRevFluids.8.124605)**I. INTRODUCTION**

Scalar quantities, such as temperature, humidity, or chemical species concentration, are mixed within a wide range of environmental and engineering flows. In the atmosphere, temperature and humidity are mixed by the turbulence generated by both shear and buoyancy, whereas temperature and salinity are mixed in the ocean within the oceanic mixed layer. In engineering devices and processes, including chemical reactors, heat exchangers and combustion, the mixing of scalars also plays a crucial role. Given that the vast majority of these flows are turbulent, a thorough understanding of the turbulent scalar mixing process is necessary to accurately predict the evolution of the concentration(s) of the scalar(s) and, ultimately, to optimize and control turbulent mixing in engineering applications.

The present study focuses on the mixing of passive scalars, where the term “passive” denotes that the evolution of the scalar does not influence the dynamics of the flow, allowing for independent treatment of the hydrodynamic field and the scalar fields it mixes. Such an assumption is reasonable and valid in many physical flows where the temperature or concentration fluctuations are

sufficiently small. These flows are governed by the continuity, Navier-Stokes, and advection-diffusion equations, where the first two equations are one-way coupled with the latter. Assuming constant thermophysical properties, the three aforementioned equations can be written as follows:

$$\frac{\partial \tilde{u}_j}{\partial x_j} = 0, \quad (1a)$$

$$\frac{\partial \tilde{u}_i}{\partial t} + \tilde{u}_j \frac{\partial \tilde{u}_i}{\partial x_j} = -\frac{1}{\rho} \frac{\partial \tilde{p}}{\partial x_i} + g_i + \nu \frac{\partial^2 \tilde{u}_i}{\partial x_j \partial x_j}, \quad (1b)$$

$$\frac{\partial \tilde{\theta}}{\partial t} + \tilde{u}_j \frac{\partial \tilde{\theta}}{\partial x_j} = \alpha \frac{\partial^2 \tilde{\theta}}{\partial x_j \partial x_j}, \quad (1c)$$

where  $\tilde{u}_j$  ( $j = 1, 2, 3$ ) are the components of the instantaneous velocity vector field,  $\rho$  is the fluid density,  $\tilde{p}$  is the instantaneous pressure,  $g_i$  represents external body forces,  $\nu$  is the kinematic viscosity,  $\tilde{\theta}$  represents the instantaneous scalar field,  $\alpha$  is the scalar's molecular diffusivity within the fluid, and repeated indices imply Einstein's summation convention. Since the overwhelming majority of flows that are encountered in practice are both turbulent and inhomogeneous, the transport of a scalar quantity in such flows is of particular interest. In this work, we therefore simulate the mixing of a passive scalar in a fully developed, high-aspect-ratio, turbulent channel flow (the simplest realization of an inhomogeneous flow) by solving the above equations.

Two important quantities in the description of turbulent scalar mixing are the scalar variance and the scalar dissipation rate, respectively defined as

$$\langle \theta^2 \rangle \equiv \langle (\tilde{\theta} - \Theta)^2 \rangle, \quad (2a)$$

$$\langle \varepsilon_\theta \rangle \equiv \alpha \left\langle \frac{\partial \theta}{\partial x_j} \frac{\partial \theta}{\partial x_j} \right\rangle, \quad (2b)$$

where  $\langle \cdot \rangle$  denotes an average and  $\theta$  is the fluctuation of a scalar about its mean ( $\Theta = \langle \tilde{\theta} \rangle$ ). The time evolutions of the scalar variance and its destruction by the scalar dissipation rate can be better understood by examining the physical processes that govern their production, transport, and destruction. These processes are described by the scalar variance and scalar dissipation rate evolution equations (also known as ‘‘budgets’’). The scalar variance budget describes the contributions of various physical mechanisms to the evolution of the scalar variance:

$$\underbrace{\frac{\partial}{\partial t} \left\langle \frac{1}{2} \theta^2 \right\rangle}_{(i)} + \underbrace{U_j \frac{\partial}{\partial x_j} \left\langle \frac{1}{2} \theta^2 \right\rangle}_{(ii)} = - \underbrace{\frac{\partial}{\partial x_j} \left\langle \frac{1}{2} u_j \theta^2 \right\rangle}_{(iii)} + \underbrace{\alpha \frac{\partial^2}{\partial x_j^2} \left\langle \frac{1}{2} \theta^2 \right\rangle}_{(iv)} - \underbrace{\langle u_j \theta \rangle \frac{\partial \Theta}{\partial x_j}}_{(v)} - \underbrace{\alpha \left\langle \frac{\partial \theta}{\partial x_j} \frac{\partial \theta}{\partial x_j} \right\rangle}_{(vi)}. \quad (3)$$

Similarly, the scalar dissipation rate budget describes the contributions of the various physical mechanisms to the evolution of the scalar dissipation rate:

$$\underbrace{\frac{\partial \langle \varepsilon_\theta \rangle}{\partial t}}_{(i)} + \underbrace{U_j \frac{\partial \langle \varepsilon_\theta \rangle}{\partial x_j}}_{(ii)} = - \underbrace{2\alpha \frac{\partial U_j}{\partial x_i} \left\langle \frac{\partial \theta}{\partial x_i} \frac{\partial \theta}{\partial x_j} \right\rangle}_{(iii)} - \underbrace{2\alpha \frac{\partial \Theta}{\partial x_j} \left\langle \frac{\partial u_j}{\partial x_i} \frac{\partial \theta}{\partial x_i} \right\rangle}_{(iv)} - \underbrace{2\alpha \left\langle u_j \frac{\partial \theta}{\partial x_i} \right\rangle \frac{\partial^2 \Theta}{\partial x_i \partial x_j}}_{(v)} \\ - \underbrace{2\alpha \left\langle \frac{\partial u_j}{\partial x_i} \frac{\partial \theta}{\partial x_i} \frac{\partial \theta}{\partial x_j} \right\rangle}_{(vi)} + \underbrace{\alpha \frac{\partial^2 \langle \varepsilon_\theta \rangle}{\partial x_j^2}}_{(vii)} - \underbrace{\frac{\partial}{\partial x_j} \langle u_j \varepsilon_\theta \rangle}_{(viii)} - \underbrace{2\alpha^2 \left\langle \frac{\partial^2 \theta}{\partial x_i \partial x_j} \frac{\partial^2 \theta}{\partial x_i \partial x_j} \right\rangle}_{(ix)}. \quad (4)$$

The physical interpretation of each term in these budgets will be provided later.

An analysis of  $\langle \theta^2 \rangle$  and  $\langle \varepsilon_\theta \rangle$  can provide insight into the evolution of a system from an unmixed state to a mixed one and, more importantly, into the physical mechanisms that contribute to the mixing process. The path that a system takes in approaching the mixed state can depend on a number

of factors. One of these factors is the starting state of the system (i.e., the initial condition), which can determine the rate at which mixing occurs [1–4]. Consequently, a better understanding of how to organize or construct the initial scalar field to achieve the desired rate of mixing can be advantageous in many fields. Immediate applications may include processes in which the rapid mixing of scalars yields numerous benefits, such as the mixing of fuel and air in combustion engines, the mixing of heat in heat exchangers, or the mixing of various chemical reactants and/or products in chemical reactors. Given that the effects of scalar-field initial conditions on the mixing process are not yet fully understood, the present work aims to study the evolutions of various scalar fields—subjected to different initial conditions—as they are mixed by identical hydrodynamic fields, such that any observed differences can *only* be attributed to the differences in the scalar fields’ initial conditions.

## II. LITERATURE REVIEW

Scalar mixing has been a topic of extensive research over the years given its prominence in both natural phenomena and engineering applications, spanning many fields. On the one hand, laminar mixing is of interest in the pharmaceutical, food, polymer, biotechnological industries, and, more recently, in micro- or nanofluidic applications. On the other hand, turbulent mixing is of interest in atmospheric, oceanic and fluvial phenomena, combustion or propulsion, and chemical engineering applications, to name a few.

Mixing in laminar regimes is generally poor because the fluid motion is dominated by viscous forces. Therefore, satisfactory laminar mixing must be induced by appropriate stirring. The study of laminar mixing began with the pioneering work by Aref (1984 and 2002), who introduced the concept of chaotic advection. Aref’s work [5,6] stimulated numerous studies, mainly within the dynamical system community, on laminar mixing (e.g., Hobbs and Muzzio [1], Ottino [7], Alvarez *et al.* [8], Szalai and Muzzio [9], Gleeson [10], Gouillart *et al.* [11], Phelps and Tucker [12], Sturman *et al.* [13], Vikhansky and Cox [14]). Mixing induced by turbulent flows is much more effective, because a mixture is stirred efficiently by the vorticity field such that molecular mixing is accelerated by the increasingly stretched interfaces between the scalar and the surrounding fluid [15,16]. Given these beneficial features and the lack of a complete understanding of the turbulent mixing process, work on optimization and control of turbulent scalar mixing has been investigated by the combustion community, with a focus on jet mixing. However, efforts to understand the fundamental physical mechanisms governing the mixing of turbulent scalars also continue actively.

The origins of the study of turbulent scalar mixing follow Kolmogorov’s seminal work on turbulence [17,18], in which it was proposed that the advection of a scalar field by a turbulent flow would result in a field that is universal and locally isotropic at small scales [19,20]. Kolmogorov-Obukhov-Corrsin (KOC) theory [17–20] is the most prevalent theory of turbulent scalar mixing and predicts that the smallest scales of the scalar field should be statistically isotropic and independent of the largest scales of the scalar field, similarly to the predictions of Refs. [17,18] for the velocity field.

The mixing of scalars within turbulent flows has been the subject of multiple investigations over the years. Summaries of this work can be found in the reviews of Warhaft [15] and Shraiman and Siggia [21], which have highlighted, among other aspects, anomalous scaling of passive scalar fields, as well as their lack local isotropy. With regards to the latter, Sreenivasan [22] noted that the asymptotic state of a scalar in turbulent shear flows was only reached very slowly as the Reynolds number increased. And although he reported that local isotropy of scalars was not naturally present in shear flows, its existence at extremely large Reynolds numbers was not dismissed. He did state, however, that such large Reynolds numbers would be rare in terms of flows observed on Earth, whether they be natural or man-made. However, such an anomalous behavior of passive scalars was not limited to only shear flows. By studying the skewness of the probability density functions (PDFs) of the scalar gradient in homogeneous, isotropic turbulence, Pumir [23] revealed the presence of strong anisotropy of passive scalar fields. Furthermore, he observed sharp maxima of the scalar gradient, suggesting strong mixing in large regions, and occurrences of small regions with strong

scalar gradients. The existence of locally isotropic scalar fields in the limit of infinite Reynolds numbers was challenged by Warhaft [15], who demonstrated that anisotropy existed within both the inertial and dissipation ranges in the scalar field, in particular with strong intermittency in the inertial subrange. Findings from his work suggested that the large-scale properties of the scalar field were directly reflected onto its small scales.

Within the above context pertaining to scalar mixing in turbulent flows, large amounts of research have been devoted to the optimization of jet mixing, including transverse jets, which have widespread applications, particularly in energy and propulsion systems, due in part to their superior near-field mixing characteristics when compared with free jets issuing into quiescent surroundings. Applications to combustion systems include the injection of cooling air into hot combustion products or the premixing of fuel and oxidizer. Many investigations have been devoted to the optimization and control of mixing induced by transverse jets, including the work of Moussa *et al.* [24], Bowman [25], Vermeulen *et al.* [26], Margason [27], Holdeman [28], Smith and Mungal [29], Johari *et al.* [30], M'Closkey *et al.* [31], Shan and Dimotakis [32], Ekkad *et al.* [33], Sau and Mahesh [34], Karagozian [35], Gevorkyan *et al.* [36], Harris *et al.* [37], among others.

The specific motivation for the present work stems from the observations of Gubanov and Cortelezzi [3] and Germaine *et al.* [38], who noted that scalar fields are strongly affected by the initial conditions of the scalar field, even when these scalar-field initial conditions were mixed by identical hydrodynamic fields. In other words, it appears to be possible to optimize and passively control the mixing performance of certain engineering applications by constructing appropriate initial conditions. It is therefore of interest to study and investigate the nature of the physical processes that lead to such different evolutions of the scalar field to determine the initial conditions that optimize turbulent scalar mixing

Gubanov and Cortelezzi [3] addressed the problem of designing a mixing device capable of maintaining a uniform mixing quality for different scalar-field initial conditions in laminar flow. The authors compared the performance of the same mixing device, the sine flow or egg-beater flow [39], by stirring the same initial mixture using periodic [40–42], recursive symmetry-breaking [43], and short-horizon optimal [44] protocols. The periodic protocol, often used in the chemical and food industries, is the worst performer. It is the slowest mixer and, under certain initial conditions, leaves regions of unmixed fluid within the island of regular motion of the mixer. The recursive symmetry-breaking protocol, as well as other, random protocols considered by Liu *et al.* [45], were found to induce chaotic advection over the entire mixing domain and, therefore, mix faster and better than a periodic protocol. The short-horizon optimal protocols are the best performers. They produce, in the shortest time, a uniform mixing quality for all different scalar-field initial conditions considered. Protocol optimization was obtained by minimizing the mixnorm [46] over a short-horizon of a few stirring periods, where the mixnorm ( $\mu_\theta$ ) is defined as

$$\mu_\theta = \left[ \sum_{\mathbf{k} \in \mathbb{Z}^3} \frac{1}{\sqrt{1 + 4\pi^2 \|\mathbf{k}\|^2}} |\hat{\Theta}_{\mathbf{k}}(t)|^2 \right]^{1/2}, \quad (5)$$

where  $\mathbf{k}$  is the wavenumber and  $\hat{\Theta}_{\mathbf{k}}$  are the spectral coefficients of the scalar fluctuations. Note that  $\mu_\theta \geq 0$  and the mixnorm is positive semi-definite. Even minimization over a single period worked quite well. Gubanov and Cortelezzi [3] concluded that each initial condition of the scalar field was mixed efficiently, both in space and time, by a different short-horizon optimal protocol.

Germaine *et al.* [38] undertook an investigation in a three-dimensional (3D), turbulent flow. In this work, the dependence of the anisotropy of passive scalar fields on their initial conditions was studied by analyzing the evolution of the scalar field for three different initial conditions with interfaces oriented normal to the streamwise, wall-normal, and transverse directions. The authors observed the persistence of anisotropy in the fractional components of the scalar dissipation rates for the three initial conditions. Moreover, they also observed, at the final time, that the three scalar-fields showed different degrees of mixing.

The dependence of the turbulent scalar flux ( $\langle u_j \theta \rangle$ ) on scalar-field initial conditions in homogeneous turbulent shear flow was investigated by Rogers *et al.* [47]. In this work, the authors undertook direct numerical simulations of passive scalar fields arising from mean scalar gradients in three orthogonal directions to investigate the evolution of the scalar flux, with the objective of developing a model for them. The result was a gradient transport model with a second-order diffusivity tensor with one empirically determined coefficient. It was compared with the data from the authors' direct numerical simulations of homogeneous turbulent shear flow, as well as the homogeneous, isotropic, grid turbulence data of Sirivat and Warhaft [48] and data from simulations of fully developed turbulent channel flow. Given that the model was solely based on the hydrodynamic field, the scalar gradient, and the Prandtl number, it was found to better reproduce data in which the differences in the scalar-field initial conditions were "weakened" by the production of turbulence by mean shear.

The topic of optimal mixing conditions was studied by Foures *et al.* [49], who investigated optimal initial perturbations to maximize mixing of a passive scalar in a two-dimensional plane Poiseuille flow at finite Reynolds and Péclet numbers. Their work showed that energy optimization led to very weak mixing of the scalar field, while optimal mixing initial perturbations homogenized the scalar field effectively.

Vermach and Caulfield [50] built on the work of Foures *et al.* [49] in their study of optimal mixing in three-dimensional plane Poiseuille flow at high Péclet numbers. The object of their study was the identification of the optimal initial velocity-field perturbation that maximized mixing by a given time horizon. They reported their findings at two different Reynolds numbers (i.e.,  $Re = 500$  and  $Re = 3000$ ) and stated that the optimal perturbations that minimize the mixnorm for short time horizons result in better scalar-field mixing than optimal perturbations that minimize the scalar variance. Furthermore, the authors found that flows at higher Reynolds numbers mixed scalar fields to a greater extent than those at lower Reynolds numbers.

Minimization of the mixnorm was further explored in the work of Eggl and Schmid [51,52], who proposed the use of a gradient-based nonlinear optimization scheme to improve the mixing efficiency of binary fluids by moving stirrers. Two cylindrical stirrers moving on concentric circular paths were used with an iterative direct-adjoint algorithm to enhance mixing. In the work of Eggl and Schmid [51], the stirrers' shapes were held constant and not subjected to optimization for enhanced mixing. To address this additional optimization parameter, the work of Eggl and Schmid [52] investigated the optimal cross-sectional shape of the stirrers in addition to the mixing strategy to further enhance scalar mixing. The authors studied four cases in their study: (i) a base configuration that was used to compare all subsequent optimizations, (ii) optimization of the cross-sectional shape of the stirrers, (iii) optimization of the velocities of the stirrers, and (iv) combined optimization of the cross-sectional shape and velocities of the stirrers. The combined optimization of the shape and the velocity of the stirrers led to the best mixing (i.e., lowest measured mix-norm) of the binary fluids.

Optimal stirring by way of adaptive flow reorientation was studied by Lensvelt *et al.* [53], who developed a flow-control strategy to heat rapidly and uniformly a cold fluid via a hot boundary. Their research indicated that adaptive flow reorientation significantly accelerated the heating of the fluid as compared to conventional periodic schemes in terms of consistency and effectiveness. The accelerated heating was achieved by the controller via thermal plumes that extended from the heated wall into the colder fluid interior. The plumes were produced by thermal convection between two counter-rotating recirculation regions, also known as "thermals."

It has been demonstrated that there exists a dependence of the scalar mixing process on the initial scalar-field geometries. It has also been shown that by optimizing the mixing device or the stirring protocol (or both), one may mix uniformly and rapidly a given initial condition. However, the latter is often impractical in turbulent flows of engineering interest. For this reason, further investigation into the mechanisms that lead to different evolutions of the scalar fields arising from different initial conditions is merited. Deepening our understanding of these relationships will allow for better prediction and control of flows in which scalar mixing occurs.

TABLE I. Details of the numerical grids for the computation of the velocity and scalar fields. The superscript “+” indicates the normalization by the viscous length ( $\nu/u_\tau$ ) or time ( $\nu/u_\tau^2$ ) scale, and the superscripts “\*” and “•” are used for the normalization by the Kolmogorov ( $\eta$ ) and Corrsin ( $\eta_\theta$ ) length scales, respectively.

	Velocity	Scalar
$L_x \times L_y \times L_z$	$2\pi h \times 2h \times \pi h$	$2\pi h \times 2h \times \pi h$
$L_x^+ \times L_y^+ \times L_z^+$	$1187 \times 378 \times 594$	$1187 \times 378 \times 594$
$N_x \times N_y \times N_z$	$256 \times 193 \times 192$	$514 \times 195 \times 194$
$\Delta x^+, \Delta y^+, \Delta z^+$	$4.64, 0.025 - 3.1, 3.1$	$2.32, 1.96, 3.1$
$\Delta x^*, \Delta y^*, \Delta z^*$ at $y/h = 1.0$	$1.25, 0.83, 0.84$	–
$\Delta x^\bullet, \Delta y^\bullet, \Delta z^\bullet$ at $y/h = 1.0$	–	$0.50, 0.42, 0.66$

### III. NUMERICAL SIMULATIONS

The investigations herein employ numerical simulations of both the turbulent velocity and passive scalar fields, in which the latter is advected by the former. The turbulent velocity field is computed by way of direct numerical simulation (DNS) using a code entitled CHANNELFLOW [54,55] which uses spectral discretization in space (Fourier  $\times$  Chebyshev  $\times$  Fourier), and a third-order semi-implicit backwards differentiation scheme in time, with no-penetration or no-slip boundary conditions imposed at the walls of the channel ( $y = 0$  and  $y = 2h$ , where  $h$  is the half-height of the channel), and periodic boundary conditions in the streamwise ( $x$ ) and spanwise ( $z$ ) directions. Simulation of the hydrodynamic field is conducted at  $\text{Re}_\tau = 190$  over a domain of size  $2\pi \times 2 \times \pi$ , in the streamwise ( $x$ ), wall-normal ( $y$ ), and spanwise ( $z$ ) directions, respectively, with a resolution of  $256 \times 193 \times 192$ . ( $\text{Re}_\tau \equiv u_\tau h/\nu$ ,  $u_\tau \equiv \sqrt{v \times \partial U / \partial y}|_{y=0}$ ,  $h = 1$ , and  $\nu$  is the kinematic viscosity of the fluid.) The resulting turbulent velocity field is statistically steady and statistically one-dimensional, such that  $\langle U \rangle = \langle U \rangle(y)$  only.

The precomputed velocity field is used as an input to the advection-diffusion solver and is interpolated from a spectral to a finite-volume representation via spectral (exact) interpolation. A very small correction is applied to the streamwise component of the velocity field to ensure the exact divergence-free condition. The advection-diffusion equation is solved using a fully three-dimensional and cost-effective flux integral method entitled 3DFLUX [56]. The fully explicit and multidimensional nature of the approach ensures that it is free of splitting errors and provides a better convergence rate of the numerical errors when compared to commonly used one-dimensional methods. A semi-Lagrangian approach is implemented in 3DFLUX by discretizing the spatial domain on an Eulerian grid and using a Lagrangian frame of reference for temporal discretization. Solutions for the advection-diffusion equation are obtained using nonoverlapping control volumes to discretize the computational domain and estimate the flux exchanged between adjacent cells. DNS of the scalar field is undertaken on the same domain of  $2\pi \times 2 \times \pi$ , with a resolution of  $514 \times 195 \times 194$  to resolve both the large and small scales of the scalar field. It is assumed that the magnitudes of the scalar fluctuations are sufficiently small, such that the dynamics of the velocity field are independent of the scalar field, such that the scalar is deemed passive. Details of the numerical grids for the computation of the velocity and scalar fields are given in Table I, and the justification of these selections is given in Germaine *et al.* [57] (see Sec. 4 therein). To summarize their arguments, the computational domains were selected to be large enough to capture the integral scales, and the spatial resolution was chosen to be small enough to resolve, as accurately as possible, the dissipative scales. The domain size selected herein is the same as in Kawamura *et al.* [58], Moser *et al.* [59], and Schwertfirm and Manhart [60]. Galantucci and Quadrio [61] performed DNSs on a smaller domain [ $L_x = 4.19h$ ,  $L_y = 2h$ ,  $L_z = 2.09h$ , with  $\text{Re}_\tau = 160$  and Schmidt number ( $Sc \equiv \nu/D$ ) equal to 1.0] at three increasingly resolved scalar fields, which they deemed low, medium, and high. The low resolution was comparable to that of most DNSs of wall-bounded flows in which scalars were mixed, whereas the high resolution one employed cell

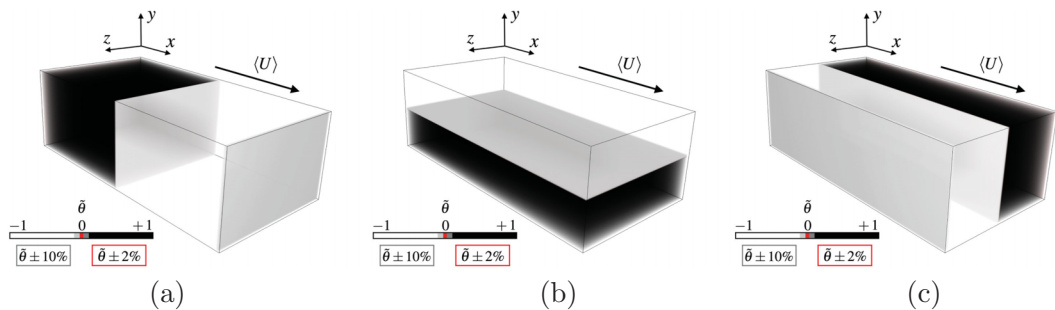


FIG. 1. The three scalar-field initial conditions studied herein. (a)  $IC_x$ ; (b)  $IC_y$ ; (c)  $IC_z$ . (Imagery generated using VAPOR.)

sizes that were consistently smaller than the Kolmogorov length scale evaluated at the wall. The spatial resolution denoted medium fell in between the other two. Leveraging their results, we chose a grid consistent with their medium resolution for our simulations at  $Re_\tau = 190$  and  $Pr (\equiv \nu/\alpha) = 0.7$ , which also satisfactorily reproduced prior experimental results [57].

The evolution in time of the mixing will be studied for three different scalar-field initial conditions,  $IC_x$ ,  $IC_y$ , and  $IC_z$ , as depicted in Fig. 1. These fields consist of two equal volumes of uniform concentrations,  $\tilde{\theta} = +1$  (black) and  $-1$  (white), separated by two interfaces (due to the periodic boundary conditions in  $x$  and  $z$ ) of total area  $4\pi h^2$  ( $=2 \times 2h \times \pi h$ ) for  $IC_x$  and  $8\pi h^2$  ( $=2 \times 2h \times 2\pi h$ ) for  $IC_z$  and a single interface of area  $2\pi^2 h^2$  ( $=2\pi h \times \pi h$ ) for  $IC_y$ . The transition from one region of uniform concentration to another (i.e., from  $\tilde{\theta} = +1$  to  $\tilde{\theta} = -1$ ) follows a smooth step function. The scalar concentration across the interface(s) is defined by the function

$$\tilde{\theta} = \sin\left(\frac{\pi}{2} + \frac{x_i - x_{\text{int}}}{L_{\text{int}}}\pi\right),$$

where  $x_i$  is the coordinate normal to the interface,  $x_{\text{int}}$  is the coordinate that marks the beginning of the interface, and  $L_{\text{int}}$  is the width of the interface. The width of the interface was set to be equal to approximately 10% of the channel height for all three scalar-field initial conditions, such that  $L_{\text{int}} = 0.2h$ . All fields have zero mean concentration. Note that all three scalar fields are subjected to identical turbulent velocity fields, and thus any differences in the evolutions of the three scalar fields are the sole result of the orientations of the interfaces defining the initial scalar fields relative to that of the mean velocity field.

The simulations conducted herein were run on the Digital Research Alliance of Canada's Graham cluster. CHANNELFLOW's ability to utilize message passing interface allowed for the hydrodynamic simulation to be run across multiple nodes using a total of 128 cores in parallel. For 3DFLUX, Intel's Thread Building Blocks library was used to take advantage of multithreading across 32 CPU cores located on the same node for each of the three scalar-field initial conditions. For both the velocity and scalar-field simulations, the computations were performed using Intel E5-2683 v4 Broadwell CPUs running at 2.1 GHz.

The CPU time required for the hydrodynamic field simulation was 0.12 CPU years, corresponding to a wall-clock time of 8 h. For each of the three scalar-field simulations, the CPU time required was 1.84 CPU years, corresponding to a wall-clock time of three weeks. The scalar field was saved every time step to provide a sufficient temporal resolution for the scalar-field simulations. This resulted in a set of 40 000 files that were 240 MB in size, totalling 9.6 TB. For each of the three scalar-field initial condition simulations, the output consisted of 40 000 files of 156 MB each, resulting in a total of 18.7 TB across all three scalar-field initial conditions. In total, the storage requirements were 28.3 TB for the velocity and scalar fields combined.

## IV. RESULTS

The simulation results are presented in this section. However, before discussing the main results in Sec. IV.C, we first present the averaging schemes employed herein in Sec. IV.A, since the scalar fields studied in this work are both statistically unsteady and multidimensional. Then, in Sec. IV.B, we discuss the (statistically steady and one-dimensional) velocity field that advects the (statistically unsteady and multidimensional) scalar field.

### A. Averaging schemes

Given the complex nature of the velocity and scalar fields studied in this work, the ensuing analysis of the statistics requires special care to treat the hydrodynamic and scalar fields meaningfully. Although the velocity field is statistically stationary, the scalar fields are all unsteady, as they evolve from their initial states to the mixed state. The velocity field is also inhomogeneous in the wall-normal ( $y$ ) direction. Additionally, the homogeneity of the three scalar fields are different. The scalar field resulting from the  $IC_x$  initial condition is statistically homogeneous in the  $z$  direction (only). That resulting from the  $IC_y$  initial condition is statistically homogeneous in the  $x$  and  $z$  directions. Last, the scalar field resulting from the  $IC_z$  initial condition is statistically homogeneous in the  $x$  direction (only).

The underlying symmetries and ensuing statistical (in-)homogeneities associated with the different initial conditions, as well as the statistical nonstationary nature of the scalar field, must be considered when analyzing the results. A primary consequence of this fact is that one can no longer simply volume-average the terms in Eqs. (3) and (4) if one wants to examine the evolution(s) of all their constituent terms, because some of the various, relevant terms become zero when volume averaged. Moreover, there is no “universal” approach to spatial averaging that will not eliminate some of the pertinent terms in describing the evolutions of the scalar fields. For example, were one to average scalar-field statistics in the  $z$  direction, certain terms in Eq. (4)—such as production by the mean scalar gradient—will become zero for the  $IC_z$  case only, because  $\partial\langle\cdot\rangle_z/\partial z = 0$  due to the statistical homogeneity in the  $z$  direction. Because volume-averaging is no longer feasible, averaging will be taken over (spatial) planes (at specific locations within the channel) to investigate the terms in Eqs. (3) and (4). However, because the amount of data in a plane is (much) less than in a volume, the statistical convergence of the data is reduced. To address this, local time averages will also be employed (i.e., averaging statistics in time from  $\tau' = 0$  to  $\tau' = \tau$ ), which will improve convergence of the data, while retaining its time dependence. Moreover, certain analyses will also involve local spatial averages after having performed the time-average, which, when calculated in this way, do not eliminate terms and further aid convergence.

Having introduced the complexities and intricacies associated with the analysis of the results in this 3D unsteady, inhomogeneous problem, the specific averaging conventions used herein will now be discussed. The simplest averaging scheme that will be used in the following subsections is volume averaging, which will be denoted by  $\langle\cdot\rangle_{x,y,z} = \langle\cdot\rangle_V$ . Volume-averaging is ideal for studying the scalar dissipation rate, which in this context will capture the average rate at which the scalar variance is destroyed in the channel as a function of time. However, when analyzing the scalar variance and scalar dissipation rate budgets, planar averaging will be used. For each of the scalar-field initial conditions, spatial averages will be taken over planes (at specific locations) that are parallel to the interface(s) separating the two initial scalar concentrations.

In the case of  $IC_x$ , averages will be taken over  $y$ - $z$  planes, such that the averaging used is denoted as  $\langle\cdot\rangle = \langle\cdot\rangle_{y,z}$ . This approach ensures that the terms analyzed in Eqs. (3) and (4) for  $IC_x$  are functions of both time and space in the inhomogeneous direction ( $x$ ) only. A similar approach is taken for the other two scalar fields, such that the averaging used for the  $IC_y$  initial condition is denoted by  $\langle\cdot\rangle = \langle\cdot\rangle_{x,z}$  and that for the  $IC_z$  initial condition is given by  $\langle\cdot\rangle = \langle\cdot\rangle_{x,y}$ . Thus, for all three scalar fields, the terms in the scalar variance and scalar dissipation rate budgets will be functions of both time and

a single spatial direction, corresponding to the direction of inhomogeneity for the respective scalar field.

As previously noted, local time averaging (i.e., a running time average) is used to increase the convergence of the terms in the aforementioned equations. To this end, the temporal average defined at the time  $\tau$  is taken over the time interval  $0 \leq \tau' \leq \tau$ . This approach is denoted in the appropriate figures using the notation

$$\frac{1}{\tau} \int_{\tau'=0}^{\tau'=\tau} \text{Term} \, d\tau',$$

where Term represents a term in the budget that has already been spatially averaged over its respective plane. Last, a final approach taken to improve the convergence and capture the evolution(s) of the various terms over the entire channel is to average the terms over all planes along the direction of inhomogeneity. For example, in the case of  $\text{IC}_x$ , the terms are averaged over  $y$ - $z$  planes which are normal to the  $x$  axis and will change in that direction. For optimal convergence, the averages of the terms (in the  $\text{IC}_x$  case) are calculated using all  $y$ - $z$  planes normal to the  $x$  axis along the entire length of the channel. When used, this scheme is denoted as follows:

$$\frac{1}{L} \int_{l=0}^{l=L} \text{Term} \, dl,$$

where  $L$  represents the distance along the direction of inhomogeneity (the channel length in this case). In certain instances, both approaches are combined, such that the final averaging scheme is given via a combination of the two aforementioned schemes, and is denoted by

$$\frac{1}{L} \frac{1}{\tau} \int_{l=0}^{l=L} \int_{\tau'=0}^{\tau'=\tau} \text{Term} \, d\tau' \, dl.$$

## B. Velocity field

In this section, the hydrodynamic (velocity) field generated via CHANNELFLOW is (i) presented and (ii) validated against published data generated via DNS for similar simulations. Validation is performed by comparing profiles of the mean longitudinal velocity and the root-mean-square (rms) value of the three velocity components as functions of the wall-normal distance with the works of Refs. [57,62] in Fig. 2.

As observed in Fig. 2(a), the mean longitudinal velocity follows a linear profile in the viscous sublayer ( $y^+ < 5$ ) and a logarithmic profile in the log-law region ( $30 \leq y^+ \leq 100$ ). The present data agrees with established analytic profiles as well as the results of Refs. [57,62]. The rms profiles of the three velocity components are also validated against the works of Refs. [57,62] in Fig. 2(b). Validation against the work of Ref. [57] is provided to confirm that the CHANNELFLOW 2.0 simulation for the present work was configured correctly and consistent with results obtained using the prior version (CHANNELFLOW 1.0). The peak observed in the near-wall region for the  $u_{\text{rms}}^+$  profile corresponds to peak turbulent activity in the near-wall region. Excellent agreement is observed once again between the present work and the prior published data for the rms profiles.

## C. Scalar field

Before proceeding to a presentation of the main results of this work, which pertain to the evolution of the scalar fields within identical inhomogeneous (channel) flows, but subjected to different scalar-field initial conditions, we briefly discuss the validation of 3DFLUX—the code used herein to solve the advection-diffusion equation. 3DFLUX has been extensively validated in prior works, so the present discussion will only provide a summary of this validation. To validate and verify the code, Germaine *et al.* [56] employed five numerical tests to assess the convergence rate and accuracy of 3DFLUX. These tests included (i) four 2D and 3D numerical tests, in which the simulations were compared with analytical solutions to the test cases, as well as

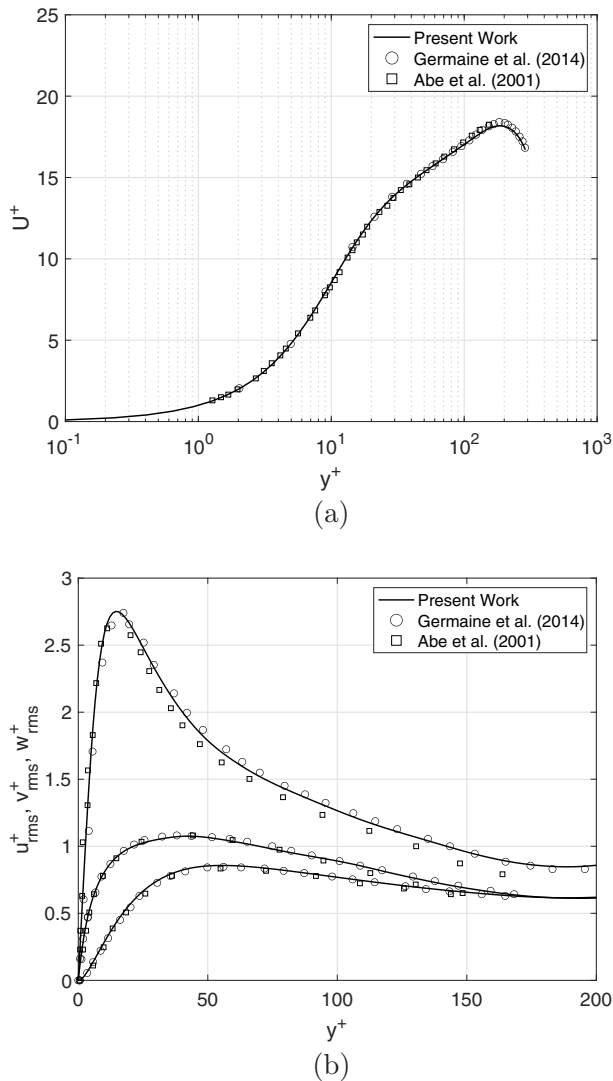


FIG. 2. Mean streamwise component of the velocity field (a) and the rms values of the three velocity field components (b) and comparisons with the work of Refs. [57,62].

(ii) a three-dimensional direct numerical simulation of a real experiment in which a thermal plume was released in a fully developed, high-aspect-ratio turbulent channel flow facility [63]. Further validation of 3DFLUX was undertaken in Germaine *et al.* [57], in which 3DFLUX simulations were compared with experimental measurements of the scalar dissipation rate and related statistics in the flow downstream of a thermal line source located within a turbulent channel flow.

### 1. Scalar variance and dissipation rate

The three scalar-field initial conditions visualized in Fig. 1 were subjected to the action of identical hydrodynamic fields over the time interval  $0 \leq \tau (\equiv u_\tau t/h) \leq 7$ . The use of identical velocity fields for advecting and diffusing all three scalar-field initial conditions ensures that any differences observed in the evolutions of these fields will be a sole result of the orientation of the

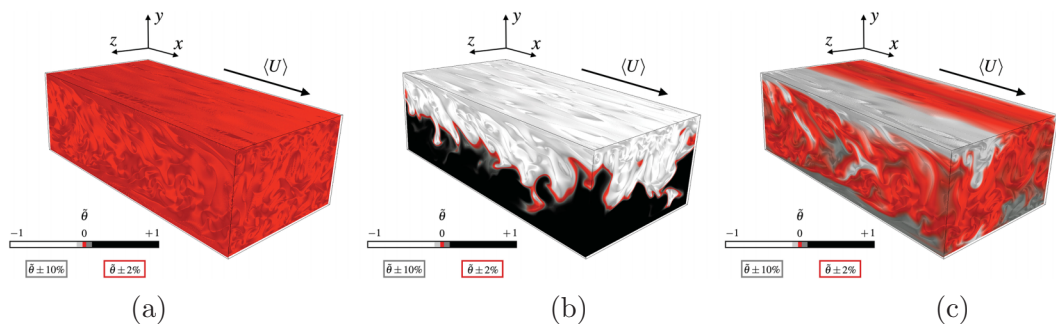


FIG. 3. Concentration distributions generated at  $\tau = 7$  by the action of the same turbulent channel flow on the three scalar-field initial conditions. (a)  $IC_x$ ; (b)  $IC_y$ ; (c)  $IC_z$  (Imagery generated using VAPOR.)

initial scalar field. Figure 3 plots the scalar field distributions that result from the action of the turbulent channel flow on the scalar-field initial conditions at  $\tau = 7$ .

From Fig. 3, it is readily observed that the scalar field resulting from the  $IC_x$  initial condition [Fig. 3(a)] is the best mixed, whereas that resulting from the  $IC_y$  initial condition [Fig. 3(b)] is the least mixed. This is already an intriguing result and indicates that the initial conditions can strongly influence the subsequent mixing. Moreover, it is worth reiterating that all three scalar-field initial conditions were composed of equal parts “black fluid” (i.e., scalar with an initial concentration  $\tilde{\theta} = +1$ ) and “white fluid” (i.e., scalar with an initial concentration  $\tilde{\theta} = -1$ ). Thus, one can already conclude that the rate at which mixing will occur in such an inhomogeneous flow (as is the flow in all real devices) is highly dependent on the initial configuration of the two quantities being mixed.

To further investigate the evolution of the scalar field, we plot the time evolutions of the volume-averaged scalar variance and the volume-averaged scalar dissipation rate for the three scalar-field initial conditions in Fig. 4. The time evolutions of the volume-averaged scalar variance,  $\langle \theta^2 \rangle_V$ , observed in Fig. 4(a) for the three initial conditions show that the fastest mixing occurs in the  $IC_x$  case (in which  $\langle \theta^2 \rangle_V$  decays most rapidly), whereas the slowest mixing occurs in the  $IC_y$  case. These quantitative observations are consistent with the qualitative ones depicted in Fig. 3. Moreover, the observed decay of  $\langle \theta^2 \rangle_V$  is approximately exponential in time, with decay rates dependent on the initial conditions of the scalar field. These trends can be compared with those of the volume-averaged scalar dissipation rates in Fig. 4(b). These demonstrate that, at larger times, the fastest decrease in  $\langle \varepsilon_\theta \rangle_V$  occurs for  $IC_x$ , corresponding to the most efficient mixing, and the slowest corresponding to  $IC_y$ . At these larger times, the decrease of  $\langle \varepsilon_\theta \rangle_V$  also appears to be exponential. However, at shorter times,  $\langle \varepsilon_\theta \rangle_V$  increases, presumably due to the stretching and stirring of the interface between the two (i.e., the “black” and “white”) scalar fields, which results in production of  $\langle \varepsilon_\theta \rangle_V$ . Note that the values of  $\langle \varepsilon_\theta \rangle_V$  for the  $IC_x$  and  $IC_z$  cases peak around  $\tau \approx 1/3$ , whereas the peak in  $\langle \varepsilon_\theta \rangle_V$  for the  $IC_y$  case occurs later, around  $\tau \approx 2/3$ . Furthermore, the highest peak of  $\langle \varepsilon_\theta \rangle_V$  occurs for  $IC_x$ , indicating the largest production of the scalar dissipation rate, whereas the smallest peak occurs the  $IC_y$  initial condition.

The peak values for  $\langle \varepsilon_\theta \rangle_V$  denote the time at which the rate of destruction of the scalar variance is maximum. As  $\langle \varepsilon_\theta \rangle_V$  tends to zero at larger values of  $\tau$ , the rate at which the scalar variance is destroyed begins to slow down, with the  $IC_x$  case corresponding to the slowest rate of scalar variance destruction. The larger values of  $\langle \theta^2 \rangle_V$  for case  $IC_y$  depict how the scalar field resulting from that initial condition is the furthest from the mixed state. Moreover, the larger values of  $\langle \varepsilon_\theta \rangle_V$  for  $IC_y$  at later times are associated with the larger rates of destruction of the remaining  $\langle \theta^2 \rangle_V$ , resulting in larger values of its dissipation.

Based on the evolution of  $\langle \varepsilon_\theta \rangle_V$  over time, one can hypothesize that the rate at which the scalar variance is destroyed increases initially as a result of the initial interface being stretched and stirred by the flow for all three initial conditions. After a maximum rate of destruction of the scalar variance

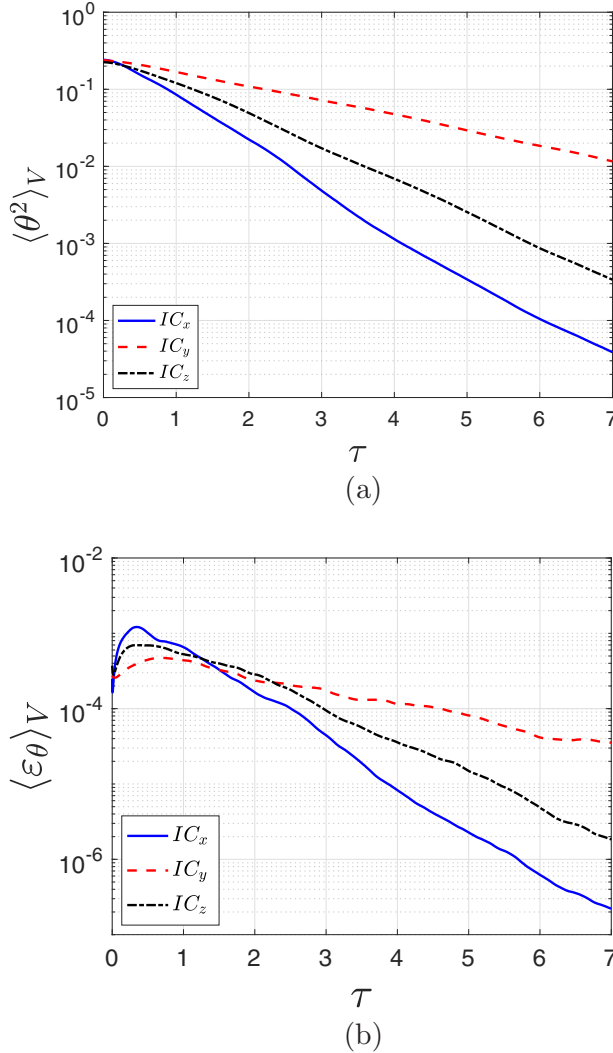


FIG. 4. Time evolutions of the volume-averaged scalar variance (a) and the volume-averaged scalar dissipation rate (b) for the three scalar fields resulting from the three initial conditions.

has been achieved, there is a monotonic decay in the rate of scalar variance destruction for all three initial conditions as the concentration distributions of the three scalar fields approach a mixed state with increasing time. Ultimately, the value of the scalar dissipation rate will tend to zero because there will be no scalar variance remaining that can be destroyed.

## 2. Scalar variance budget

To better understand the evolution of  $\langle \varepsilon_\theta \rangle$  presented in Fig. 4(b), we start by studying the scalar variance budget [Eq. (3)], which describes the contributions of different physical mechanisms involved in the evolution of the scalar variance. These mechanisms involve the mean, turbulent, and molecular transports of the scalar variance, in addition to its production and destruction. It should be noted that  $\langle \varepsilon_\theta \rangle$  appears explicitly as a term in the scalar variance budget, as it quantifies the rate of destruction of the scalar variance. Thus, analysis of all the terms in the scalar variance budget

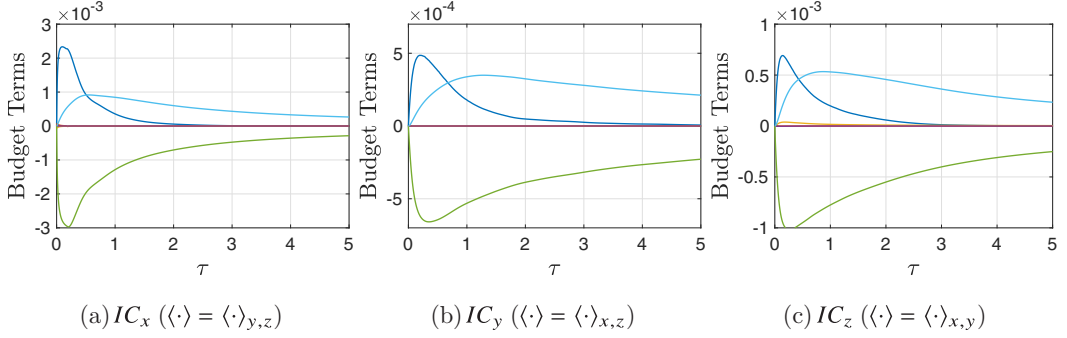


FIG. 5. Evolution in time of the space and time averages of all six terms in the scalar variance budget in which statistical moments ( $\langle \cdot \rangle$ ) are assessed in planes parallel to the initial location of the interface in the initial condition. (a)  $IC_x$  with  $\frac{1}{L_x} \frac{1}{\tau} \int_0^{L_x} \int_0^\tau \text{Term } d\tau' dx$ , (b)  $IC_y$  with  $\frac{1}{2h} \frac{1}{\tau} \int_0^{2h} \int_0^\tau \text{Term } d\tau' dy$ , and (c)  $IC_z$  with  $\frac{1}{L_z} \frac{1}{\tau} \int_0^{L_z} \int_0^\tau \text{Term } d\tau' dz$ . Note the different scales of the vertical axes.

will provide further insight into the physical processes that contribute to the evolution of the scalar variance.

To this end, Fig. 5 plots the contributions of the terms in the budget of  $\langle \frac{1}{2} \theta^2 \rangle$ . To assist the reader, a legend corresponding to the budget's six terms is also provided in Table II. Statistical moments ( $\langle \cdot \rangle$ ) for this analysis are assessed in planes parallel to the initial location of the interface in the initial condition. The first observation to be made from Fig. 5 is that the rate of change in time of the scalar variance (i) is dominated by the production (v) and destruction (vi) of  $\langle \frac{1}{2} \theta^2 \rangle$ . The production of the scalar variance results from the stretching of the interface, which creates or enhances mean scalar gradients, thus increasing the scalar variance at early times, as indicated by the increase in term (i) of the scalar variance budget.

A second set of observations from Fig. 5 is drawn by considering the relative magnitudes of the terms for the different initial conditions. One observes that the largest peak for the production of the scalar variance [i.e., term (v)] occurs for  $IC_x$ , while the smallest peak occurs for  $IC_y$ . Furthermore, the largest peak in the destruction of the scalar variance (i.e.,  $\langle \varepsilon_\theta \rangle$ ) also occurs for  $IC_x$ , with the smallest peak again being associated with the  $IC_y$  initial condition. The highest magnitude for  $\langle \varepsilon_\theta \rangle$  observed for the  $IC_x$  initial condition in Fig. 5 is consistent with the highest peak observed in the volume-averaged scalar dissipation rate in Fig. 4(b). Similarly, the smallest magnitude of  $\langle \varepsilon_\theta \rangle$  observed in the scalar variance budget is consistent with the smallest observed peak in the volume-averaged plot of  $\langle \varepsilon_\theta \rangle$ , as seen in Fig. 4(b).

TABLE II. Legend for the various terms in the budget for the scalar variance.

Color	Term no.	Term	Physical interpretation
<span style="color: blue;">—</span>	(i)	$\frac{\partial}{\partial t} \langle \frac{1}{2} \theta^2 \rangle$	Time rate of change of $\langle \frac{1}{2} \theta^2 \rangle$
<span style="color: orange;">—</span>	(ii)	$U_j \frac{\partial}{\partial x_j} \langle \frac{1}{2} \theta^2 \rangle$	Mean flow advection of $\langle \frac{1}{2} \theta^2 \rangle$
<span style="color: yellow;">—</span>	(iii)	$\frac{\partial}{\partial x_j} \langle \frac{1}{2} u_j \theta^2 \rangle$	Turbulent advection of $\langle \frac{1}{2} \theta^2 \rangle$
<span style="color: purple;">—</span>	(iv)	$-\alpha \frac{\partial^2}{\partial x_j^2} \langle \frac{1}{2} \theta^2 \rangle$	Molecular transport of $\langle \frac{1}{2} \theta^2 \rangle$
<span style="color: green;">—</span>	(v)	$\langle u_j \theta \rangle \frac{\partial \theta}{\partial x_j}$	Production of $\langle \frac{1}{2} \theta^2 \rangle$
<span style="color: cyan;">—</span>	(vi)	$\alpha \langle \frac{\partial \theta}{\partial x_j} \frac{\partial \theta}{\partial x_j} \rangle$	Destruction of $\langle \frac{1}{2} \theta^2 \rangle$ (i.e., $\langle \varepsilon_\theta \rangle$ )

Last, it becomes apparent from Fig. 5 that the production and destruction of the scalar variance is most dominant at early times, when each of the three systems are the least mixed. Although scalar variance increases at early times due to a larger production of  $\frac{1}{2}\langle\theta^2\rangle$  than its destruction, its rate of change goes to zero once the production and destruction of  $\frac{1}{2}\langle\theta^2\rangle$  become balanced at later times. When spatially averaged over the respective direction of inhomogeneity, the contributions from mean, molecular, and turbulent transport are nonexistent for all three scalar-field initial conditions. Consequently, a long-term equilibrium exists in Fig. 5 between the production and destruction of  $\frac{1}{2}\langle\theta^2\rangle$ . The production and destruction terms become equal and opposite first for IC<sub>x</sub>, then for IC<sub>z</sub>, and last for IC<sub>y</sub>. Note that at  $\tau = 5$ , in the latter case, production is still larger than destruction. As the systems approach a uniformly mixed state, the production and destruction curves begin to asymptotically decay to zero.

### 3. Scalar dissipation rate budget

A more comprehensive understanding of the evolution of  $\langle\varepsilon_\theta\rangle$  can be achieved by analyzing the terms in the scalar dissipation rate budget [Eq. (4)]. Although the scalar variance budget describes the phenomena impacting the evolution of the scalar variance, the scalar dissipation rate budget describes the phenomena involved in the evolution of  $\langle\varepsilon_\theta\rangle$ . An analysis of the terms in the scalar dissipation rate budget will therefore provide insight into the contributions of various physical processes involved in the evolution of  $\langle\varepsilon_\theta\rangle$ .

To further investigate the evolutions of  $\langle\varepsilon_\theta\rangle$  depicted in Fig. 4(b), Fig. 6 plots the contributions of the terms in the budget of  $\langle\varepsilon_\theta\rangle$ . To once again assist the reader, a legend corresponding to the nine terms of Eq. (4) is given in Table III. Particular attention should be given to the different averaging schemes used in this subsection. Multiple observations can be made from the plots therein. For  $\tau > 1$ ,  $\langle\varepsilon_\theta\rangle$  is dominated by a balance between the production of  $\langle\varepsilon_\theta\rangle$  arising from turbulent vortex stretching and dissipation of  $\langle\varepsilon_\theta\rangle$  by molecular processes, as first predicted in Ref. [64]. However, further details also bear noting. First, when considering the relative magnitudes of the various terms for the different initial conditions, it is clear that the magnitudes of the terms for the IC<sub>x</sub> condition are the largest, followed by those corresponding to the IC<sub>z</sub> initial condition. Those corresponding to the IC<sub>y</sub> initial condition are the smallest. Using the peak value of the molecular dissipation of  $\langle\varepsilon_\theta\rangle$  [i.e., term (ix), light green line] as a reference, its value for IC<sub>x</sub> is  $4 \times 10^{-5}$ , for IC<sub>z</sub> is  $2 \times 10^{-5}$ , and for IC<sub>y</sub> is  $1 \times 10^{-5}$ . Thus the larger values of all terms in the scalar field arising from the IC<sub>x</sub> initial condition lead to the largest peaks of  $\langle\varepsilon_\theta\rangle$ , as well as the fastest decay rates of  $\langle\varepsilon_\theta\rangle$ , consistent with Fig. 4(b). Moreover, the converse holds for IC<sub>y</sub>, which experiences the lowest peak value of  $\langle\varepsilon_\theta\rangle$  and slowest decay rates. Second, one can observe in Fig. 6 that the two dominant terms (production of  $\langle\varepsilon_\theta\rangle$  by turbulent vortex stretching and molecular dissipation of  $\langle\varepsilon_\theta\rangle$ ) peak at later times for IC<sub>y</sub> (at  $\tau > 1$ ) than they do for the IC<sub>x</sub> and IC<sub>z</sub> cases (which peak at  $\tau < 1$ ). This behavior is also consistent with the evolutions of  $\langle\varepsilon_\theta\rangle$  in Fig. 4(b), noted above. Another interesting observation is that the production of  $\langle\varepsilon_\theta\rangle$  by the mean scalar gradients goes to zero at  $\tau \approx 0.5$  for IC<sub>x</sub>, while it contributes to production over the entire time interval considered for IC<sub>y</sub> and IC<sub>z</sub>. This indicates that in the case of IC<sub>x</sub>, the mean scalar gradients are quickly destroyed by the rapid mixing taking place over the entire domain. In the case of IC<sub>y</sub> and IC<sub>z</sub>, large unmixed regions still survive at  $\tau = 5$ . The presence of these large regions of unmixed scalars is responsible for the persistence of mean scalar gradients.

To further investigate the budget of the scalar dissipation rate for the three initial conditions, the time evolution of terms when spatially averaged over a single  $y$ - $z$  plane is plotted in Fig. 7. Note that the plane over which the spatial averaging is performed in Fig. 7 is parallel to the initial interface between the “black” and “white” fluids in the IC<sub>x</sub> case, and located at the midplane of the channel in the  $x$  direction ( $x/L_x = 0.5$ ), i.e., the location of one of the two interfaces between the “black” and “white” fluids at  $\tau = 0$  for IC<sub>x</sub>. In Fig. 7, it is first worth noting the qualitative similarities of the evolutions of the terms in the  $\langle\varepsilon_\theta\rangle$  budget for the IC<sub>y</sub> and IC<sub>z</sub> initial conditions. These two subfigures exhibit similar behaviours due to the absence of terms associated with spatial gradients

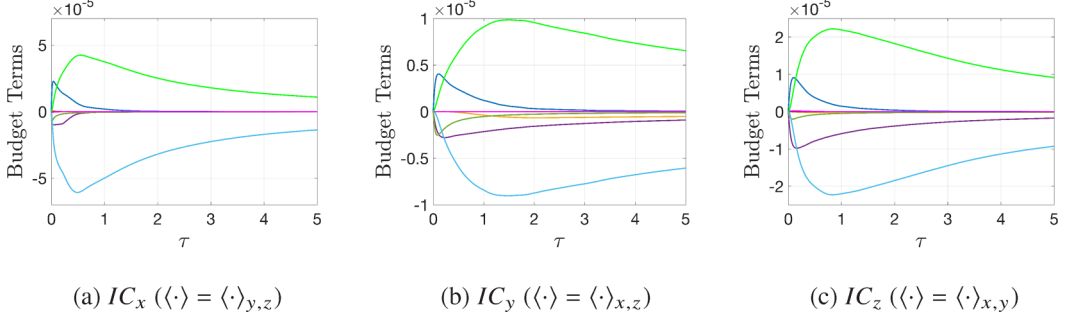


FIG. 6. Evolution in time of the space and time averages of all nine terms in the scalar dissipation rate budget in which statistical moments  $\langle \cdot \rangle$  are assessed in planes parallel to the initial location of the interface in the initial condition. (a)  $IC_x$  with  $\frac{1}{L_x} \frac{1}{\tau} \int_0^{L_x} \int_0^\tau \text{Term } d\tau' dx$ , (b)  $IC_y$  with  $\frac{1}{2h} \frac{1}{\tau} \int_0^{2h} \int_0^\tau \text{Term } d\tau' dy$ , and (c)  $IC_z$  with  $\frac{1}{L_z} \frac{1}{\tau} \int_0^{L_z} \int_0^\tau \text{Term } d\tau' dz$ . Note the different scales of the vertical axes.

of statistical moments in the directions of the averaging in the respective figures. We also note that analogous similarities are observed when reproducing the equivalent of Fig. 7, but spatial averaging in the other two ( $x$ - $z$  and  $x$ - $y$ ) midplanes. To this end, Figs. 8 and 9 plot the temporal evolutions of the scalar dissipation rate budget terms when averaged along  $x$ - $z$  and  $x$ - $y$  planes, respectively, at the other two midplanes of the channel. The averaging schemes used ensure that the relevant budget terms are conserved for  $IC_y$  in the case of  $x$ - $z$  averaging and for  $IC_z$  in the case of  $x$ - $y$  averaging. In contrast to Figs. 7(b) and 7(c), Fig. 7(a) is dominated at early times by mean-flow advection of  $\langle \varepsilon_\theta \rangle$  and turbulent advection of  $\langle \varepsilon_\theta \rangle$ . This will be further discussed with respect to Fig. 10, which follows.

To investigate the evolution of the terms in the  $\langle \varepsilon_\theta \rangle$  budget that are *not* subjected to such an artifact as that discussed with respect to Figs. 7 and 10 plots the evolution in time of the scalar dissipation rate budget terms assessed on the midplane corresponding to the initial location of the interface for the three initial conditions. [To make this clear, we emphasize that Fig. 10(a) is a reproduction of Figs. 7(a) and 10(b) is the same as Figs. 8(b) and 10(c) is the same as Fig. 9(c).] Comparison of the subfigures in Fig. 10 reveals that Fig. 10(a), which corresponds to the  $IC_x$  initial condition, is significantly different from those corresponding to  $IC_y$  [Fig. 10(b)] and  $IC_z$  [Fig. 10(c)], which are quite similar. Although the dominant terms in Figs. 10(b) and 10(c) are the molecular

TABLE III. Legend for the various terms in the budget of the scalar dissipation rate.

Color	Term no.	Term	Physical interpretation
<span style="color: blue;">—</span>	(i)	$\frac{\partial}{\partial \tau} \langle \varepsilon_\theta \rangle$	Time rate of change of $\langle \varepsilon_\theta \rangle$
<span style="color: orange;">—</span>	(ii)	$\langle U_j \rangle \frac{\partial}{\partial x_j} \langle \varepsilon_\theta \rangle$	Mean flow advection of $\langle \varepsilon_\theta \rangle$
<span style="color: yellow;">—</span>	(iii)	$2\alpha \frac{\partial \langle U_j \rangle}{\partial x_i} \langle \frac{\partial \theta}{\partial x_i} \frac{\partial \theta}{\partial x_j} \rangle$	Production of $\langle \varepsilon_\theta \rangle$ by mean velocity gradients
<span style="color: purple;">—</span>	(iv)	$2\alpha \frac{\partial \langle \Theta \rangle}{\partial x_j} \langle \frac{\partial u_j}{\partial x_i} \frac{\partial \theta}{\partial x_i} \rangle$	Production of $\langle \varepsilon_\theta \rangle$ by mean scalar gradients
<span style="color: green;">—</span>	(v)	$2\alpha \frac{\partial^2 \langle \Theta \rangle}{\partial x_i \partial x_j} \langle u_j \frac{\partial \theta}{\partial x_i} \rangle$	Mixed production of $\langle \varepsilon_\theta \rangle$
<span style="color: cyan;">—</span>	(vi)	$2\alpha \langle \frac{\partial u_j}{\partial x_i} \frac{\partial \theta}{\partial x_i} \frac{\partial \theta}{\partial x_j} \rangle$	Production of $\langle \varepsilon_\theta \rangle$ by turbulent vortex stretching
<span style="color: red;">—</span>	(vii)	$-\alpha \frac{\partial^2}{\partial x_j \partial x_j} \langle \varepsilon_\theta \rangle$	Molecular transport of $\langle \varepsilon_\theta \rangle$
<span style="color: magenta;">—</span>	(viii)	$\frac{\partial}{\partial x_j} \langle u_j \varepsilon_\theta \rangle$	Turbulent advection of $\langle \varepsilon_\theta \rangle$
<span style="color: lightgreen;">—</span>	(ix)	$2\alpha^2 \langle \frac{\partial^2 \theta}{\partial x_i \partial x_j} \frac{\partial^2 \theta}{\partial x_i \partial x_j} \rangle$	Molecular dissipation of $\langle \varepsilon_\theta \rangle$

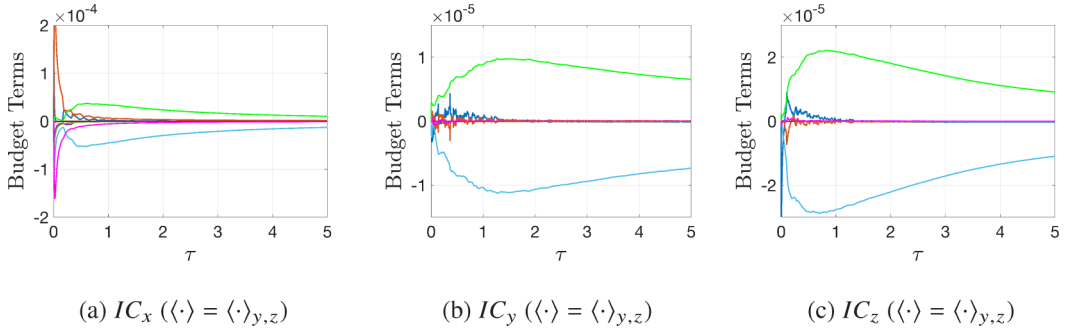


FIG. 7. Evolution in time of the time-averages of all nine terms in the scalar dissipation rate budget in which statistical moments  $\langle \cdot \rangle$  are assessed on the  $y$ - $z$  plane at  $x/L_x = 0.50$ , i.e.,  $\frac{1}{\tau} \int_0^\tau \text{Term } d\tau'$ , where all averages  $\langle \cdot \rangle$  in Term are given by  $\langle \cdot \rangle = \langle \cdot \rangle_{y,z}$ .

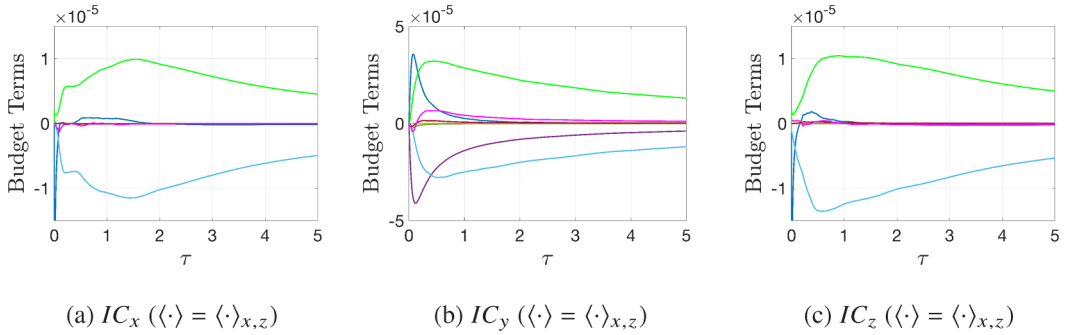


FIG. 8. Evolution in time of the time averages of all nine terms in the scalar dissipation rate budget in which statistical moments  $\langle \cdot \rangle$  are assessed on the  $x$ - $z$  plane at  $y/h = 1$ , i.e.,  $\frac{1}{\tau} \int_0^\tau \text{Term } d\tau'$ , where all averages  $\langle \cdot \rangle$  in Term are given by  $\langle \cdot \rangle = \langle \cdot \rangle_{x,z}$ .

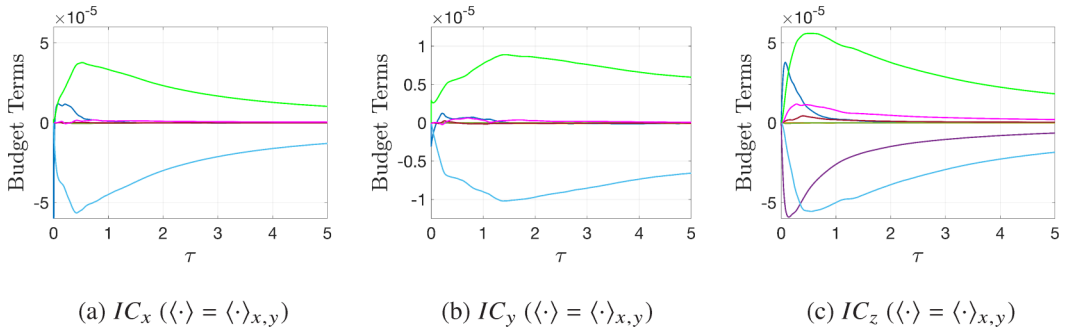


FIG. 9. Evolution in time of the time averages of all nine terms in the scalar dissipation rate budget in which statistical moments  $\langle \cdot \rangle$  are assessed on the  $x$ - $y$  plane at  $z/L_z = 0.50$ , i.e.,  $\frac{1}{\tau} \int_0^\tau \text{Term } d\tau'$ , where all averages  $\langle \cdot \rangle$  in Term are given by  $\langle \cdot \rangle = \langle \cdot \rangle_{x,y}$ .

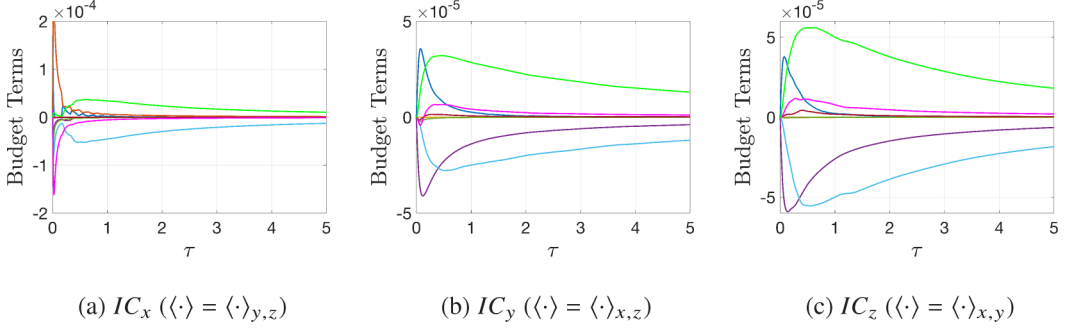


FIG. 10. Evolution in time of the time averages of all nine terms in the scalar dissipation rate budget in which statistical moments  $\langle \cdot \rangle$  are assessed on the midplane corresponding to the initial location of the interface in the initial condition:  $\frac{1}{\tau} \int_0^\tau \text{Term} d\tau'$ . (a)  $IC_x$  with statistical moments evaluated over the  $y$ - $z$  plane at  $x/L_x = 0.50$ , (b)  $IC_y$  with statistical moments evaluated over the  $x$ - $z$  plane at  $y/h = 1$ , and (c)  $IC_z$  with statistical moments evaluated over the  $x$ - $y$  plane at  $z/L_z = 0.50$ .

dissipation of  $\langle \varepsilon_\theta \rangle$ , the production of  $\langle \varepsilon_\theta \rangle$  by turbulent vortex stretching, production of  $\langle \varepsilon_\theta \rangle$  by mean scalar gradients, the rate of change of  $\langle \varepsilon_\theta \rangle$  with time, and turbulent advection of  $\langle \varepsilon_\theta \rangle$ , Fig. 10(a) is distinctly different. Of particular note is the importance played by mean-flow advection of  $\langle \varepsilon_\theta \rangle$  at early times, which is dominant for  $\tau < 0.2$  and balanced by turbulent advection of  $\langle \varepsilon_\theta \rangle$  for  $IC_x$ . Given that fully developed turbulent channel flow must be unidirectional, the absence of the mean-flow advection term in the other directions is to be expected. However, the early dominance of this term is noteworthy. In this respect, consideration of the evolution in time of the interface(s) between the “black” and “white” fluids is beneficial. For the  $IC_y$  case, the  $\langle \Theta \rangle = 0$  plane will not change in time and will be advected along the  $y/h = 1$  plane as the flow evolves but remaining at the same location as the initial interface. However, the evolution of the scalar field in time is quite different for  $IC_x$ . The interface remains “anchored” to the walls due to the no-slip condition and is strongly stretched in the  $x$  direction by the mean flow, while being stirred by the turbulence. Thus as the interface is advected downstream, it can “blow by” a given downstream location multiple times. This effect can be observed by the oscillations in the unsteady term (dark blue line) and to a lesser degree the mean flow advection terms (red line) in Fig. 10(a). It is worth noting that the period of the observed oscillation is indeed equal to half of the channel’s “flow-through” time [i.e.,  $\frac{1}{2} \tau_{FT} \equiv$

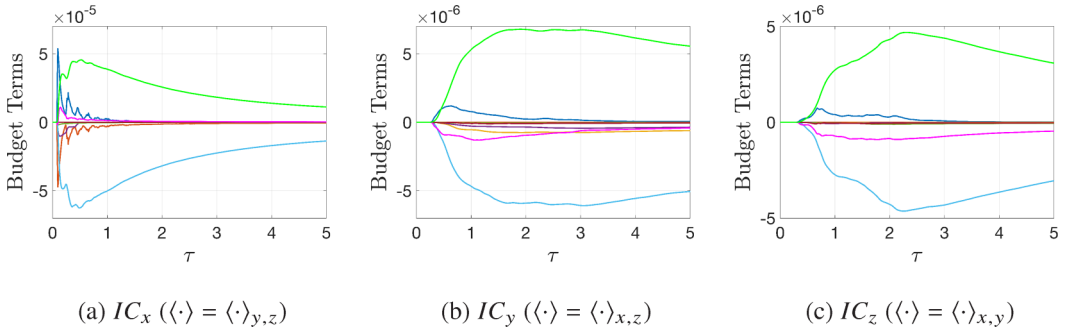


FIG. 11. Evolution in time of the time-averages of all nine terms in the scalar dissipation rate budget in which statistical moments  $\langle \cdot \rangle$  are assessed in planes parallel to the initial location of the interface in the initial condition but away from the midplane:  $\frac{1}{\tau} \int_0^\tau \text{Term} d\tau'$ . (a)  $IC_x$  with statistical moments evaluated over the  $y$ - $z$  plane at  $x/L_x = 0.25$ , (b)  $IC_y$  with statistical moments evaluated over the  $x$ - $z$  plane at  $y/h = 0.5$ , and (c)  $IC_z$  with statistical moments evaluated over the  $x$ - $y$  plane at  $z/L_z = 0.25$ .

$\frac{1}{2}(L_x/\langle U \rangle_{y/h=1})u_\tau/h = 0.17]$ . With respect to  $IC_z$ , the  $\Theta = 0$  plane will be advected downstream the midplane of the channel ( $z = 0.5L_z$ ), although its top and bottom edges will remain at the walls of the channel, thus emulating aspects of both  $IC_x$  and  $IC_y$ . The anchoring of the interfaces to the walls also subjects them to strong turbulent activity that is encountered in the near-wall region. As such,  $IC_x$  and  $IC_z$  experience enhanced scalar mixing due to the strong turbulent activity arising from the anchoring of the interfaces to the walls.

Given that the results in Fig. 10 are all averages taken at the three midplanes of the channel, they are somewhat anomalous. For example, when averaging in the  $x$  and  $z$  directions at  $y/h = 1$  [as is the case in Fig. 10(b)], there can be no contribution to  $\langle \varepsilon_\theta \rangle$  arising from production by the mean velocity gradient, because  $\partial \langle U \rangle / \partial y = 0$  at that one location (and no other). Thus it bears investigating the budget of the scalar dissipation rate for the three initial conditions at non-mid-plane locations. To this end, the evolutions of the terms in the budget of the scalar dissipation rate are plotted for  $IC_x$  spatially averaged over an  $y$ - $z$  plane located at  $x/L_x = 0.25$  in Fig. 11(a), for  $IC_y$  spatially averaged over an  $x$ - $z$  plane located at  $y/h = 0.5$  in Fig. 11(b), and for  $IC_z$  spatially averaged over an  $x$ - $y$  plane located at  $z/L_z = 0.25$  in Fig. 11(c). The aforementioned periodic passing of the interfaces over the measurement plane for the  $IC_x$  case is even more prominent in Fig. 11(a). However, Figs. 11(b) and 11(c) also reveal another phenomenon that explains the slower evolutions of  $\langle \varepsilon_\theta \rangle$  for the  $IC_y$  and  $IC_z$  cases. In these two non-mid-plane cases, one observes an initial period of ‘‘inactivity.’’ The initial period in which the terms in the budget of  $\langle \varepsilon_\theta \rangle$  are effectively zero results from the interface having not yet ‘‘reached’’ the measurement location. In these two cases, the interface can only travel laterally by the action of the turbulence, given that there is no mean velocity in the  $y$  and  $z$  directions. This phenomenon (i) is not observed for the  $IC_x$  case, because the interface can be advected by the nonzero mean flow, and (ii) further explains the slower evolutions of  $\langle \varepsilon_\theta \rangle$  for the  $IC_y$  and  $IC_z$  cases, given that regions located increasingly far away from the interface experience a delay before they begin to mix. This latter effect therefore serves to retard the total mixing, because the interface surface is not normal to the mean velocity vector.

## V. CONCLUSIONS

The motivation behind the present work was a lack of understanding of the effects of scalar-field initial conditions on the evolution of the scalar fields in inhomogeneous turbulent flows. Very often in both natural and engineering applications, it is desirable to either promote or delay the mixing of a scalar in a turbulent flow. To that end, it is beneficial to better understand the role of scalar-field initial or injection conditions in the evolution of the field from an unmixed state to a mixed one.

Direct numerical simulations were conducted for three different scalar-field initial conditions to study their effects on the evolutions of the scalar variance and scalar dissipation rate budgets. The flow considered in this work was a fully developed turbulent channel flow to provide relevance with the abundance of inhomogeneous flows encountered in the real world.

Results of the DNSs showed that there was a clear dependence of the mixing on the scalar-field initial conditions. Evolution of the volume-averaged scalar dissipation rate in time showed that the case with the initial scalar interface aligned normal to the direction of the mean velocity vector ( $IC_x$ ) experienced the fastest mixing of the three initial conditions. The case where the initial interface was aligned parallel to the mean velocity vector and was not restrained by the walls ( $IC_y$ ) experienced the slowest mixing.

An increase in  $\langle \varepsilon_\theta \rangle_V$  was observed at early times, and attributed to the stretching of the interface, with a decay of the scalar dissipation rate following the peaks. The largest peak of  $\langle \varepsilon_\theta \rangle_V$  for the  $IC_x$  case corresponded to the fastest rate of destruction of scalar variance observed across all three cases. As the mixing progressed, the values of  $\langle \varepsilon_\theta \rangle_V$  tended towards zero, with  $IC_x$  approaching the mixed state sooner than the other initial conditions.

Analysis of the scalar variance budget provided further insight into the mixing resulting from the different initial conditions. It was found that the magnitudes of production and destruction of  $\langle \frac{1}{2}\theta^2 \rangle$  were highest for  $IC_x$  and lowest for  $IC_y$ . Furthermore, the production and destruction terms were

most dominant at early times ( $\tau < 1$ ) and asymptotically decayed to zero as the systems approached a mixed state.

Analysis of the terms in the budget of the scalar dissipation rate showed that the magnitude of the terms was consistent with both large values of  $\langle \varepsilon_\theta \rangle$  and rapid decay rates of  $\langle \varepsilon_\theta \rangle$ . Once again, the magnitudes of the production(s) and destruction of  $\langle \varepsilon_\theta \rangle$  were the highest for the  $IC_x$  case and the lowest for  $IC_y$ . The strong stretching of the initial interface by the mean velocity gradient was a key factor in promoting the production of  $\langle \varepsilon_\theta \rangle$  in  $IC_x$ . Furthermore, a period of inactivity away from the initial locations of the interfaces for  $IC_y$  and  $IC_z$  was observed and attributed to the lack of mean-flow advection normal to the initial interface. Last, interfaces that intersected the channel walls ( $IC_x$  and  $IC_z$ ) were also subjected to strong near-wall turbulent activity, further enhancing the mixing.

It bears emphasizing that the strong stretching of the initial interface (that is linked to accelerated mixing) is tied to the inhomogeneity, and ensuing anisotropy, of the flow. Although scalar mixing within homogeneous flows can also exhibit dependencies on the scalar-field initial conditions (e.g. Rogers *et al.* [47], Sirivat and Warhaft [48]), the distortion of the interface by the mean flow in the present case is directly related to the differences in mean velocity across the flow, which are amplified by the (i) inhomogeneity of the flow (that arises from the no-slip condition at the walls) and (ii) orientation of the initial scalar interface relative to the mean velocity vector. In homogeneous, isotropic turbulence, initial scalar interfaces will not be distorted by the mean flow, and only by the turbulent velocity fluctuations, akin to the  $IC_y$  initial condition. In homogeneous (but anisotropic) turbulent shear flow, the inhomogeneity of the flow can stretch the interface. However, it cannot be subjected to as strong of a distortion as in an inhomogeneous flow.

These observations suggest that the orientation of the initial interface with respect to the mean velocity vector plays a key role in the evolution of the scalar field. The mixing and stirring that occurs therein is influenced by the stretching (or lack thereof) of the initial interface and also by the action of the near-wall turbulent activity (which is absent in a homogeneous flow). The mechanisms that contribute to the production and destruction of the scalar dissipation rate greatly benefit from having the movement of the interface being restrained by the walls while being strongly stretched by the mean flow. Thus, it is recommended that for a wall-bounded flow, the scalar interfaces should be aligned normal to the direction of the mean velocity vector to enhance the stretching of the interface and thus promote scalar mixing.

#### ACKNOWLEDGMENTS

Support for this work was graciously provided by the Natural Sciences and Engineering Research Council of Canada (Grant No. RGPIN-2018-05848). Funding for M.S. was provided by the Natural Sciences and Engineering Research Council of Canada (Canada Graduate Scholarships Master's program) and the Fonds de recherche du Québec, Nature et technologies (Master's research scholarships). This research was also enabled in part by support provided by Calcul Québec and the Digital Research Alliance of Canada.

- 
- [1] F. J. Hobbs and F. J. Muzzio, Effects of injection location, flow ratio and geometry on kenics mixer performance, *Am. Inst. Chem. Engng J.* **43**, 3121 (1997).
  - [2] J. M. Zalc, E. S. Szalai, and F. J. Muzzio, Mixing dynamics in the smx static mixer as a function of injection location and flow ratio, *Polym. Eng. Sci.* **43**, 875 (2003).
  - [3] O. Gubanov and L. Cortelezzi, Sensitivity of mixing optimization to the geometry of the initial scalar field, in *Analysis and Control of Mixing with an Application to Micro and Macro Flow Processes*, edited by L. Cortelezzi and I. Mezić (Springer, Vienna, 2009), p. 369.
  - [4] M. Farazmand, Optimal initial condition of passive tracers for their maximal mixing in finite time, *Phys. Rev. Fluids* **2**, 054601 (2017).

- 
- [5] H. Aref, Stirring by chaotic advection, *J. Fluid Mech.* **143**, 1 (1984).
- [6] H. Aref and M. S. E. El Naschie, *Chaos Applied to Fluid Mixing* (Pergamon Press, Oxford, 1995).
- [7] J. M. Ottino, *The Kinematics of Mixing: Stretching, Chaos, and Transport* (Cambridge University Press, Cambridge, 1989).
- [8] M. M. Alvarez, F. J. Muzzio, S. Cerbelli, A. Adrover, and M. Giona, Self-similar spatiotemporal structure of intermaterial boundaries in chaotic flows, *Phys. Rev. Lett.* **81**, 3395 (1998).
- [9] E. S. Szalai and F. J. Muzzio, Fundamental approach to the design and optimization of static mixers, *Am. Inst. Chem. Eng. J.* **49**, 2687 (2003).
- [10] J. P. Gleeson, Transient micromixing: examples of laminar and chaotic stirring, *Phys. Fluids* **17**, 100614 (2005).
- [11] E. Gouillart, J.-L. Thiffeault, and M. D. Finn, Topological mixing with ghost rods, *Phys. Rev. E* **73**, 036311 (2006).
- [12] J. H. Phelps and C. L. Tucker, Lagrangian particle calculations of distributive mixing: Limitations and applications, *Chem. Eng. Sci.* **61**, 6826 (2006).
- [13] R. Sturman, J. M. Ottino, and S. Wiggins, *The Mathematical Foundations of Mixing: The Linked Twist Map as a Paradigm in Applications: Micro to Macro, Fluids to Solids* (Cambridge University Press, Cambridge, 2006).
- [14] A. Vikhansky and S. M. Cox, Conditional moment closure for chemical reactions in laminar chaotic flows, *Am. Inst. Chem. Eng. J.* **53**, 19 (2007).
- [15] Z. Warhaft, Passive scalars in turbulent flows, *Annu. Rev. Fluid Mech.* **32**, 203 (2000).
- [16] K. Sreenivasan, Turbulent mixing: A perspective, *Proc. Natl. Acad. Sci. USA* **116**, 18175 (2019).
- [17] A. N. Kolmogorov, The local structure of turbulence in incompressible viscous fluid for very large Reynolds numbers, *Dokl. Akad. Nauk. SSSR* **30**, 301 (1941a).
- [18] A. N. Kolmogorov, Dissipation of energy in the locally isotropic turbulence, *Dokl. Akad. Nauk. SSSR* **32**, 16 (1941b).
- [19] A. Obukhov, Structure of the temperature field in turbulent flows, *Akad. Nauk. SSSR* **13**, 58 (1949).
- [20] S. Corrsin, On the spectrum of isotropic temperature fluctuations in an isotropic turbulence, *J. Appl. Phys.* **22**, 469 (1951).
- [21] B. Shraiman and E. Siggia, Scalar turbulence, *Nature (London)* **405**, 639 (2000).
- [22] K. Sreenivasan, On local isotropy of passive scalars in turbulent shear flows, *Proc. R. Soc. London, Ser. A* **434**, 165 (1991).
- [23] A. Pumir, A numerical study of the mixing of a passive scalar in three dimensions in the presence of a mean gradient, *Phys. Fluids* **6**, 2118 (1994).
- [24] Z. M. Moussa, J. W. Trischka, and S. Eskinazi, The nearfield in the mixing of a round jet with a cross-stream, *J. Fluid Mech.* **80**, 49 (1977).
- [25] C. T. Bowman, Control of combustion-generated nitrogen oxide emissions: Technology driven by regulation, *Symposium (International) on Combustion* **24**, 859 (1992).
- [26] P. J. Vermeulen, P. Grabinski, and V. Ramesh, Mixing of an acoustically excited air jet with a confined hot crossflow, *Trans. ASME: J. Eng. Gas Turbin. Power* **114**, 46 (1992).
- [27] R. J. Margason, Fifty Years of Jet in Cross-Flow Research Presented at Computational and Experimental Assessment of Jets in Cross-Flow (2nd ed.), AGARD-CP 534, Winchester, UK (1993).
- [28] J. D. Holdeman, Mixing of multiple jets in a confined subsonic cross-flow, *Prog. Energy Combust. Sci.* **19**, 31 (1993).
- [29] S. H. Smith and M. G. Mungal, Mixing, structure, and scaling of the jet in crossflow, *J. Fluid Mech.* **357**, 83 (1998).
- [30] H. Johari, M. Pacheco-Tougas, and J. Hermanson, Penetration and mixing of fully modulated turbulent jets in crossflow, *AIAA J.* **37**, 842 (1999).
- [31] R. T. M'Closkey, J. M. King, L. Cortelezzi, and R. K. Karagozian, The actively controlled jet in crossflow, *J. Fluid Mech.* **452**, 325 (2002).
- [32] J. Shan and P. Dimotakis, Reynolds-number effects and anisotropy in transverse-jet mixing, *J. Fluid Mech.* **566**, 47 (2006).

- [33] S. V. Ekkad, S. Ou, and R. B. River, Effect of jet pulsation and duty cycle on film cooling from a single jet on a leading edge model, *J. Turbomachinery* **128**, 564 (2006).
- [34] R. Sau and K. Mahesh, Optimization of pulsed jets in crossflow, *J. Fluid Mech.* **653**, 365 (2010).
- [35] A. R. Karagozian, Transverse jets and their control, *Prog. Energy Combust. Sci.* **36**, 531 (2010).
- [36] L. Gevorkyan, T. Shoji, D. R. Getsinger, O. I. Smith, and A. R. Karagozian, Transverse jet mixing characteristics, *J. Fluid Mech.* **790**, 237 (2016).
- [37] E. W. Harris, T. Shoji, A. Besnard, S. G. Schein, R. T. M'Closkey, L. Cortelezzi, and A. R. Karagozian, Effects of controlled vortex generation and interactions in transverse jets, *Phys. Rev. Fluids* **7**, 013902 (2022).
- [38] E. Germaine, L. Mydlarski, and L. Cortelezzi, Persistence of local anisotropy of passive scalars in wall-bounded flows, *Phys. Rev. Fluids* **3**, 014606 (2018).
- [39] J. G. Franjione and J. M. Ottino, The kinematics of mixing: Stretching, chaos, and transport, *Philos. Trans. R. Soc. Lond. A* **338**, 301 (1992).
- [40] H. Aref, The development of chaotic advection, *Phys. Fluids* **14**, 1315 (2002).
- [41] M. D. Finn, S. M. Cox, and H. M. Byrne, Mixing measures for a two-dimensional chaotic stokes flow, *J. Eng. Math.* **48**, 129 (2014).
- [42] E. L. Paul, V. A. Atiemo-Obeng, and S. M. E. Kresta, *Handbook of Industrial Mixing: Science and Practice* (Wiley-Interscience, New York, 2004).
- [43] J. G. Franjione, C. W. Leong, and J. M. Ottino, Symmetries within chaos: A route to effective mixing, *Phys. Fluids A* **1**, 1772 (1989).
- [44] L. Cortelezzi, A. Adrover, and M. Giona, Feasibility, efficiency and transportability of short horizon optimal mixing protocols, *J. Fluid Mech.* **597**, 199 (2008).
- [45] M. Liu, F. Muzzio, and R. Peskin, Quantification of mixing in aperiodic chaotic flows, *Chaos Solitons Fract.* **4**, 869 (1994).
- [46] G. Mathew, I. Mezić, and L. Petzold, A multiscale measure for mixing, *Physica D* **211**, 23 (2005).
- [47] M. M. Rogers, N. N. Mansour, and W. C. Reynolds, An algebraic model for the turbulent flux of a passive scalar, *J. Fluid Mech.* **203**, 77 (1989).
- [48] A. Sirivat and Z. Warhaft, The effect of a passive cross-stream temperature gradient on the evolution of temperature variance and heat flux in grid turbulence, *J. Fluid Mech.* **128**, 323 (1983).
- [49] D. Foures, C. Caulfield, and P. Schmid, Optimal mixing in two-dimensional plane Poiseuille flow at finite Péclet number., *J. Fluid Mech.* **748**, 241 (2014).
- [50] L. Vermach and C. Caulfield, Optimal mixing in three-dimensional plane Poiseuille flow at high Péclet number, *J. Fluid Mech.* **850**, 875 (2018).
- [51] M. Eggl and P. Schmid, Mixing enhancement in binary fluids using optimised stirring strategies, *J. Fluid Mech.* **899**, A24 (2020).
- [52] M. F. Eggl and P. J. Schmid, Mixing by stirring: Optimizing shapes and strategies, *Phys. Rev. Fluids* **7**, 073904 (2022).
- [53] R. Lensvelt, M. Speetjens, and H. Nijmeijer, Fast fluid heating by adaptive flow reorientation, *Int. J. Therm. Sci.* **180**, 107720 (2022).
- [54] J. F. Gibson, J. Halcrow, and P. Cvitanović, Visualizing the geometry of state space in plane Couette flow, *J. Fluid Mech.* **611**, 107 (2008).
- [55] J. F. Gibson, Channelflow: A spectral Navier-Stokes simulator in C++, *licensed under the GNU GPL*, Technical Report ( University of New Hampshire, Durham, 2010), <http://channelflow.org/>.
- [56] E. Germaine, L. Mydlarski, and L. Cortelezzi, 3DFLUX: A high-order fully three-dimensional flux integral solver for the scalar transport equation, *J. Comput. Phys.* **240**, 121 (2013).
- [57] E. Germaine, L. Mydlarski, and L. Cortelezzi, Evolution of the scalar dissipation rate downstream of a concentrated line source in turbulent channel flow, *J. Fluid Mech.* **749**, 227 (2014).
- [58] H. Kawamura, K. Ohsaka, H. Abe, and K. Yamamoto, DNS of turbulent heat transfer in channel flow with low to medium-high prandtl number fluid, *Int. J. Heat Fluid Flow* **19**, 482 (1998).
- [59] R. D. Moser, J. Kim, and N. N. Mansour, Direct numerical simulation of turbulent channel flow up to  $Re = 590$ , *Phys. Fluids* **11**, 943 (1999).

- [60] F. Schwertfirm and M. Manhart, DNS of passive scalar transport in turbulent channel flow at high Schmidt numbers, *Int. J. Heat Fluid Flow* **28**, 1204 (2007).
- [61] L. Galantucci and M. Quadrio, Very fine near-wall structures in turbulent scalar mixing, *Int. J. Heat Fluid Flow* **31**, 499 (2010).
- [62] H. Abe, H. Kawamura, and Y. Matsuo, Direct numerical simulation of a fully developed turbulent channel flow with respect to the Reynolds number dependence., *J. Fluid. Eng. T. ASME* **123**, 382 (2001).
- [63] R. Lavertu and L. Mydlarski, Scalar mixing from a concentrated source in turbulent channel flow, *J. Fluid Mech.* **528**, 135 (2005).
- [64] S. Corrsin, Remarks on turbulent heat transfer, in *Proceedings of the Iowa Thermodynamics Symposium* (State University of Iowa, Iowa City, 1953), 5.